Contents lists available at ScienceDirect

Carbon

Research Article

Resolving mobility anisotropy in quasi-free-standing epitaxial graphene by terahertz optical Hall effect

Nerijus Armakavicius [a, *], Philipp Kühne [a], Jens Eriksson [b], Chamseddine Bouhafs [a, c, d], Vallery Stanishev [a], Ivan G. Ivanov [b], Rositsa Yakimova [b], Alexei A. Zakharov [e], Ameer Al-Temimy [c], Camilla Coletti [c, d], Mathias Schubert [a, f, g], Vanya Darakchieva [a, **]

[a] Terahertz Materials Analysis Center, THeMAC, and Center for III-Nitride Technology, C3NiT - Janzén, IFM, Linköping University, SE-58183 Linköping, Sweden
[b] Department of Physics, Chemistry and Biology IFM, Linköping University, SE-58183 Linköping, Sweden
[c] Center for Nanotechnology Innovation @NEST, Istituto Italiano di Tecnologia, Piazza S Silvestro 12, 56127, Pisa PI, Italy
[d] Graphene Labs, Istituto Italiano di Tecnologia, Via Morego, 30 16163, Genova GE, Italy
[e] MAX IV Laboratory, Lund University, Fotongatan 2, 22484, Lund, Sweden
[f] Department of Electrical and Computer Engineering and Center for Nanohybrid Functional Materials, University of Nebraska-Lincoln, NE, 68508, Lincoln, USA
[g] Leibniz Institut für Polymerforschung e.V., 01069, Dresden, Germany

ARTICLE INFO

ABSTRACT

In this work, we demonstrate the application of terahertz-optical Hall effect (THz-OHE) to determine directionally dependent free charge carrier properties of ambient-doped monolayer and quasi-free-standing-bilayer epitaxial graphene on 4H−SiC(0001). Directionally independent free hole mobility parameters are found for the monolayer graphene. In contrast, anisotropic hole mobility parameters with a lower mobility in direction perpendicular to the SiC surface steps and higher along the steps in quasi-free-standing-bilayer graphene are determined for the first time. A combination of THz-OHE, nanoscale microscopy and optical spectroscopy techniques are used to investigate the origin of the anisotropy. Different defect densities and different number of graphene layers on the step edges and terraces are ruled out as possible causes. Scattering mechanisms related to doping variations at the step edges and terraces as a result of different interaction with the substrate and environment are discussed and also excluded. It is suggested that the step edges introduce intrinsic scattering in quasi-free-standing-bilayer graphene, that is manifested as a result of the higher ratio between mean free path and average terrace width parameters. The suggested scenario allows to reconcile existing differences in the literature regarding the anisotropic electrical transport in epitaxial graphene.

1. Introduction

Since its first experimental demonstration, graphene continues to attract vast attention as a consequence of its exceptional properties and rich physics that arise from the reduced dimensionality [1,2]. Growth of epitaxial graphene (EG) on the Si-face (0001) of silicon carbide (SiC) provides homogeneous monolayer (ML) and bilayer (BL) graphene at a wafer scale [3–6]. The technology has high potential for future electronic device applications and prototype electronic devices using EG on semi-insulating (SI) SiC substrates have already been demonstrated [7–10]. However, the absence of an energy band gap in ML EG was shown to result in severe shortcomings for logic devices. Another major challenge limiting widespread application of EG is the interaction of graphene with the substrate and ambient [11], which significantly affects its free charge carrier properties. It was shown that as-grown EG on Si-face SiC is typically electron doped as a result of donor surface states at the graphene/SiC interface [12,13]. This doping translates into a displacement of the Fermi energy away from the Dirac point so that the ambipolar properties of graphene cannot be exploited. Furthermore, Si-face ML EG typically exhibits significantly lower

* Corresponding author.
** Corresponding author.
E-mail addresses: nerijus.armakavicius@liu.se (N. Armakavicius), vanya.darakchieva@liu.se (V. Darakchieva).

free charge carrier mobility parameters as compared to exfoliated graphene [14,15]. The interaction with the underlying substrate renders SiC surface morphology to be an important factor for the electronic and transport properties of EG. We have shown earlier that there exists a range of optimal terrace widths which should be kept in order to maintain formation of ML EG and to avoid increase of carrier concentration [16]. It was also reported that the step-like surface morphology of SiC can cause anisotropic carrier scattering in ML EG [17]. Such anisotropic transport in EG may significantly limit its applications in electronic devices.

Interaction with the substrate can be mitigated *via* hydrogen intercalation which decouples ML EG from the substrate by rearranging the $(6\sqrt{3} \times 6\sqrt{3})R30°$ surface reconstruction layer beneath (buffer layer) into an additional graphene layer [18]. The resulting BL graphene has higher carrier mobility parameters due to reduced interaction with the substrate and is commonly regarded as quasi-free-standing-bilayer (QFS-BL) EG. Moreover, it was shown that an external electric field can induce a tunable bandgap in BL graphene [19].

Free charge carrier properties and scattering mechanisms, including anisotropic transport in ML EG have been extensively studied. Several potential mechanisms accounting for the step edge induced scattering in ML EG have been discussed in the literature. Most commonly it is assigned to a higher concentration of defects and presence of an additional graphene layer at the step edge regions [3,20–24]. In addition, it was shown that for ML EG free of BL inclusions, there is no difference between the Hall mobility in devices oriented parallel and perpendicular to the SiC steps (few nanometer high) [3]. The authors further showed that BL inclusions lead to a decrease in carrier mobility which can be directly linked to the amount of BL contained in Hall devices [3]. Inhomogeneities in the number of graphene layers can cause a mismatch between electron wavefunctions that results in a backscattering of carriers [17]. On the other hand, local conductance mapping indicates that the local resistance in ML EG over SiC steps increases with increasing step height showing ∼55% enhancement of resistance over a 1.5 nm-high step [25]. Considering that no change in mobility has been observed across and parallel to the step edges [3] the reported increase in resistance might thus be expected to follow from a respective decrease of carrier density in EG across step edges. It should be noted that the resistance enhancement over the 1.5 nm high step is comparable to that observed at the ML/BL planar junction [25].

Hoon-bae et al. have shown that the resistivity for ML EG on 4H−SiC (0001) is much higher at the 10 nm-high single step than the resistivity caused by BL stripes on ML EG transferred onto flat SiO^2/Si surface [26]. They further showed that the distribution of defects does not change at the step edge and within the terrace regions [26]. The authors attributed the substantial step edge resistivity observed for EG to a mechanical deformation of the graphene sheets, which causes $\pi - \sigma$ bonds hybridization [26]. However, other authors claim that the curvature radius of the graphene sheets over the steps is too high to cause any significant modification of the band structure [15,22]. Low et al. have employed Slater-Koster parameterized sp^3 tight-binding model calculations to show that mechanical deformation and strain induce only weak electron scattering [27]. They have demonstrated through calculations that increased separation of the EG from SiC at the step edge regions can create an abrupt variation in doping due to varying interactions with the substrate [27]. For optimized BL-free ML EG with surface steps height lower than the unit lattice of the 4H- and 6H−SiC resistivity anisotropy was reported to diminish down to 3−4% [28]. More recently, it was shown that the local resistance of BL-free ML EG varies up to 30% at room temperature

and up to 270% at 8 K [29]. The latter was attributed to a local variation in the distance to the substrate resulting in reduced resistance in ML EG for a larger distance to the SiC substrate. Both theory [27] and experiment [29] indicate that interaction with the substrate is in the core of the observed spread of experimentally determined resistances in ML EG, while different specific mechanisms explaining the origin of anisotropic transport in ML EG continue to emerge and persists to attract significant scientific interest.

Since the removal of the buffer layer changes the interaction with the substrate, it can also significantly affect the anisotropic scattering of carriers induced by the step-like surface morphology. However, in contrast to the case of ML EG, anisotropic carrier scattering has not been investigated in QFS-BL EG. There is one report, where a strong anisotropy in electrical resistivity has been detected for QFS-BL EG [22]. However, this is attributed to the presence of an additional graphene layer at the step edges [22]. D. Momeni Pakdehi et al. have studied trilayer (TL)-free QFS-BL EG and detected anisotropy in resistance induced by step-like surface morphology [30]. The authors speculated that the observed anisotropy could be related to intercalation-related effects, however, no further focus on the origin of the anisotropy was imposed [30]. At this stage, it remains unknown whether the anisotropy is induced by the variation in doping or anisotropic carrier mobility of QFS-BL EG and what are the scattering mechanisms. The answer to these questions may determine to what extent the high potential of QFS EG for application in electronic devices can be realized.

Anisotropic transport can rise from anisotropic dispersion relation resulting in anisotropic carrier effective mass along the in-plane directions; anisotropic deformation potential constants and elastic modulus, structural anisotropy, and anisotropic scattering of free charge carriers. Resolving individual anisotropic transport properties presents a significant challenge to currently available contact-based techniques although many insights in the physics of graphene have been gained. For instance, four-probe measurements provides only electrical resistivity, while nanoscale scanning probe techniques such as Kelvin probe microscopy or conductive atomic force microscopy provide maps of local work function and current, respectively. Standard electrical Hall effect measurements provide free charge carrier mobility and density but may be geometry and size dependent and require contacts and Hall bar fabrication. The latter involves multiple processing steps that may modify the material properties. Recently, we have demonstrated the contactless long-wavelength optical Hall effect to measure independently free and quantized charge carrier type, density, effective mass and mobility in graphene [31–39] and 2D electron gases [40–42]. This technique, previously identified as the optical analog of the electrical Hall effect, measures the Lorentz force-induced birefringence at mid-infrared (MIR) to terahertz (THz) frequencies in magnetic fields [43]. Here, we show for the first time the use of THz-cavity-enhanced (CE)-optical Hall effect (OHE) to determine directional dependent mobility and study the anisotropic scattering mechanisms in ML and QFS-BL EG. In case of QFS-BL EG, we observe in-plane anisotropy of the carrier (hole) mobility parameter, with lower (higher) mobility across (along) the step edges of the substrate. Isotropic carrier mobility within the experimental error bars is determined for ML EG. The results from THz-CE-OHE, atomic force microscopy (AFM), scanning Kelvin probe microscopy (SKPM), micro-Raman spectroscopy imaging (μ-RSI), low-energy electron microscopy (LEEM) and low-energy electron diffraction (LEED) allow us to draw conclusions that step edges introduce an intrinsic scattering and anisotropy of the charge carriers in QFS-BL EG, not related to the presence of any additional graphene layers, defects, effective mass anisotropy, substrate induced doping or ambient adsorbates. For ML EG with much lower

mobility and mean free path parameters, the mobility anisotropy remains hidden as a result of the higher ratio between mean free path and average terrace size parameters.

2. Method

Three sets of EG samples were grown on Si-face (0001) of 4H−SiC SI substrates by high temperature sublimation in an argon (Ar) atmosphere. The growth conditions were tuned to achieve homogeneous ML coverage [44]. The growth temperature was 2000 °C using Ar pressure of 900 mbar for all sets of samples, and only the temperature, at which Ar was introduced was different for each set in order to shift the temperature at which the buffer layer forms. The latter has been predicted to affect the quality of graphene [45]. To produce QFS-BL EG, one of the ML EG samples from each set was annealed in hydrogen environment as described in Ref. [18]. Each of the three sample sets consists of ML and corresponding QFS-BL EG. All samples have been stored and transported in between the measurements at ambient conditions.

The number of graphene layers and their distribution across the samples were determined using reflectance mapping [46]. Details about the reflectivity mapping and thickness determination can be found in Ref. [46]. LEEM and micro-LEED studies were performed at aberration corrected low energy electron microscope (Elmitec GmbH) installed at MAXPEEM beamline (MAXIV synchrotron, Lund, Sweden). Before LEEM and micro-LEED measurements, the samples were annealed in ultrahigh vacuum at first at 450 °C for half an hour and then at 500 °C for 1 h.

THz-CE-OHE measurements were performed at ambient conditions for all sets of samples using the custom-built THz ellipsometer and OHE instrument at the THz Materials Analysis Center [37]. The OHE is the high frequency analog of the classical electrical Hall effect, and describes the magnetic field induced optical birefringence generated by free charge carriers under the influence of the Lorentz force and can be measured by Mueller matrix ellipsometry [43,47]. In CE-OHE a backside cavity between the sample and a highly reflective surface is employed to enhance the OHE signatures in the ellipsometry spectra [39,42]. The THz-CE-OHE measurements were carried out at room temperature in the frequency range of 720−960 GHz using a neodymium permanent magnet ($|\vec{B}| = 0.55$ T) at 45° angle of incidence and three different values for the magnetic field of − 0.55 T, + 0.55 T and 0 T. The THz-CE-OHE data were analyzed using a three-layer optical model consisting of SI 4H−SiC substrate, graphene layer and cavity. A bare SI 4H−SiC substrate prior to graphene growth was measured and analyzed with a parameterized model dielectric function (MDF) accounting for phonon mode contributions [43]. The resulting best-match MDF of SiC was used without any changes in the subsequent data analysis. The dielectric function of the graphene layer is modeled accounting for the contributions of free charge carriers using a classical Drude term as described in Ref. [43]. For more details about the THz-CE-OHE non-linear least-squares data analysis, we refer the reader to the Supplementary information.

The micro-Raman spectroscopy imaging (μ-RSI) measurements were performed using an Acton spectrometer equipped with a Pylon CCD detector at ambient conditions. The samples were excited with a 532 nm continuous wave frequency doubled Nd:Yag laser through a ×100 objective (N.A. 0.9). The samples were mounted on a three-axis piezoelectric stage to ensure an optimized positioning and focusing of the laser spot. The FWHM of the focused laser spot was around 400 nm. The μ-RSI spectra of EG were obtained by subtracting the Raman 4H−SiC reference spectrum from the collected spectra.

Scanning Kelvin probe microscopy (SKPM) measurements were performed using AFM (Dimension 3100, Digital Instruments), which uses an interleave lift mode to record the surface potential. The measurements were performed using conductive, platinum/iridium coated Si tips (Nanosensors PPP-EFM-20) with resonance frequencies between 45 kHz and 115 kHz. To record the surface potential, the tip follows a stored surface topography at a constant lift height of 10−20 nm above the sample, while an AC voltage of 3000 mV was applied to the tip at the resonance frequency of the tip cantilever (ω). The tip DC bias is adjusted to nullify the tip oscillation at ω, which is caused by the contact potential difference (δV_{CPD}) between the tip and the sample surface. The resulting image is a map of the variations in the δV_{CPD} between the tip and the graphene, with the variations in the δV_{CPD} assumed here to be due to changes in the surface work function ϕ_s. All the SKPM measurements were performed in ambient conditions.

3. Results and discussion

Reflectivity mapping and LEEM confirmed a homogeneous number of layers for all samples with single layer for ML EG and BL graphene for the QFS-BL EG samples, respectively (Fig. 1 and Suppl. Inf. Fig. S3). Only small inclusions of thicker graphene - BL and TL, respectively, were observed. The typical layer homogeneity is 99%, with the exception for one sets of the samples, where the growth time was increased, resulting in 92% layer homogeneity.

For brevity, we present results for single set of ML and QFS-BL EG samples, because similar results on the free-charge carrier properties are obtained for all sets from the THz-CE-OHE. Fig. 2 shows representative AFM images (a), (f), and the experimental and the best-match-calculated THz-CE-OHE Mueller matrix spectra for different in-plane (azimuth) orientations (b) - (e), (g) - (j), for one of the sets of ML [(a) - (e)] and QFS-BL [(f) - (j)] EG samples. The angles $\varphi_0, \varphi_0 + 30°$, $\varphi_0 + 60°$ and $\varphi_0 + 90°$ indicate the in-plane rotation of the samples with respect to the plane of incidence (Suppl. Inf. Fig. S1). The magneto-optic birefringence, causing THz polarization mode conversion, due to magneto-optical response of the free charge carriers within the EG layers is reflected in the off-diagonal-block Mueller matrix spectra (M_{ij} where $ij = 13, 23, 31, 32$; see Fig. 2 and Suppl. Inf. Fig. S2). The amplitudes and lineshapes of the spectral features observed in the spectra at a given magnetic field are determined only by the free charge carrier properties of graphene and are highly sensitive to their in-plane anisotropy [43]. The Mueller matrix spectra of the off-diagonal-block M_{23} and M_{32} elements for the ML EG sample [Fig. 2(b)−(e)] are nearly identical ($M_{23} \approx M_{32}$) for a given azimuth angle and remain similar for all in-plane orientations. This is a direct consequence of the electric permittivity tensor of ML EG being completely symmetric as a result of equal free charge carrier parameters along the main in-plane directions [43]. Thus, ML EG clearly exhibits an isotropic free charge carrier response. In contrast, a
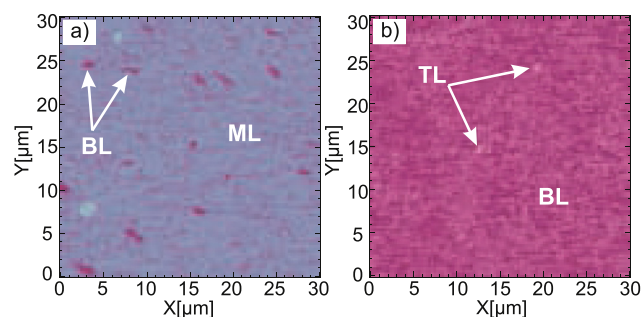
Fig. 1. Representative thickness maps of ML (a) and QFS-BL (b) EG samples obtained by reflectivity mapping. (A colour version of this figure can be viewed online.)
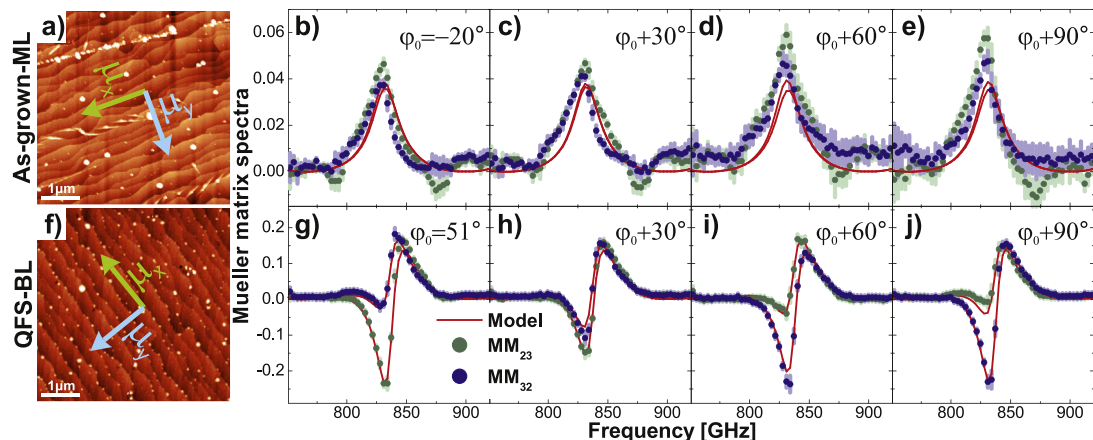
Fig. 2. Representative THz-CE-OHE Mueller matrix M_{23} and M_{32} elements spectra of the ML (b–e) and QFS-BL (g–i) EG samples at different in-plane (azimuth) orientations with 30° rotation in between the measurements. The φ_0, $\varphi_0 + 30°$, $\varphi_0 + 60°$ and $\varphi_0 + 90°$ indicates the in-plane orientation of the high mobility axis with respect to the plane of incidence (Suppl. Inf. Fig. S1). Respective AFM images depict the specific orientations of the ML (a) and QFS-BL (f) EG samples at the initial azimuth positions φ_0. The arrows in the AFM images indicate the absolute orientations of the high and low mobility axis determined from the THz-CE-OHE data analysis ($\varphi_0 = -20°$ for the ML and $\varphi_0 = 51°$ for the QFS-BL EG. (A colour version of this figure can be viewed online.)

Table 1
Free charge carrier parameters determined from the THz-CE-OHE data analysis for the representative set of ML and QFS-BLEG samples from Fig. 2. Error bars correspond to the 90% confidence interval obtained from the regression algorithm-based data analysis.

		ML	QFS-BL
Carrier density N, 10^{12} cm^{-2}		2.96±0.15	10.14±0.25
Effective mass m^*, m_0 [9.11×10^{-31} kg]		0.035[†]	0.067±0.002
Carrier type		p-type	p-type
Mobility	μ_x (along steps), cm^2/(V·s)	1133±48	2412±56
	μ_y (across steps), cm^2/(V·s)	1016±43	1927±44
Mean free path	l_x (along steps), nm	23±1	90±2
	l_y (across steps), nm	20±1	72±2

[†] The m^* was coupled to the N using the relation reported in Ref. [52].

completely different picture is observed for the QFS-BL sample. First, for a given azimuth, the M_{23} and M_{32} spectra are different in most of the cases. $M_{ij} \neq M_{ji}$ for $ij = 13, 23, 31, 32$ can only be observed if the diagonal elements of the QFS-BL permittivity tensor are different [43], i.e. the free charge parameters along the two main in-plane directions are different. As expected in the case of such an anisotropy, a strong variation of the M_{23} and M_{32} spectra with the in-plane orientation is observed. Note that $M_{23}^{\varphi_0} \approx M_{32}^{\varphi_0+90°}$ and $M_{32}^{\varphi_0} \approx M_{23}^{\varphi_0+90°}$ (Fig. 2 (g) and (j)). Such behavior of the Mueller matrix spectra for the off-diagonal-block elements (M_{ij}, where $ij = 13, 23, 31, 32$) further confirms the in-plane anisotropy of the free charge carrier properties of QFS-BL (Suppl. Inf.).

The results on the free charge carrier type, sheet density, mobility and effective mass parameters, determined by the best-match model analysis for the two samples in Fig. 2, are summarized in Table 1. The free charge carrier type is determined to be holes in both samples, with sheet density parameters of $N_{ML} = (2.96±0.15) \times 10^{12}$ cm^{-2} and $N_{QFS-BL} = (1.014±0.025) \times 10^{13}$ cm^{-2} for ML and QFS-BL EG, respectively (Table 1). The p-type doping was also confirmed by electrical Hall effect measurements (results not shown). We attribute the observed p-type conductivity in ML EG to an ambient acceptor doping redox reaction at the graphene surface involving O$_2$, H$_2$O and CO$_2$ due to long-term exposure of samples to air [35,48]. Previously, p-type conductivity in EG ML, grown by similar sublimation techniques, has also been reported [14,31]. The observed increase in hole density in our QFS-BL by $\sim 7 \times 10^{12}$ cm^{-2} is consistent with p-type doping induced by the spontaneous polarization of the SiC substrate

[18,49,50]. Hydrogen intercalation results in termination of the SiC surface by hydrogen atoms transforming the buffer layer into the additional graphene layer. Consequently, the interface donor states associated with the buffer layer [51], acting as n-type dopants, are removed leading to further enhancement of the p-type conductivity in the QFS-BL.

The THz-CE-OHE data analysis further revealed a nearly isotropic hole mobility[1] for the ML EG and a strong in-plane anisotropy of the hole mobility parameters in the QFS-BL EG. Note that this mobility values represents an ensemble average of local mobility parameters over the entire sample area of 15 mm × 15 mm. The ML EG sample exhibit mobility parameters of $\mu_x^{ML} = 1133±48$ cm^{2}V^{-1}s^{-1} and $\mu_y^{ML} = 1016±43$ cm^{2}V^{-1}s^{-1}, which within the experimental error bars may be considered isotropic (Table 1). This result is in excellent agreement with previously reported isotropic mobility parameters along and across the step edges as determined by electrical Hall effect measurements in very similar type of ML EG samples grown by high-temperature sublimation [3]. The hole mobility in our QFS-BL EG increases by a factor of ~ 2 with respect to the ML EG with strongly anisotropic parameters of $\mu_x^{QFS-BL} = 2412±56$ cm^{2}V^{-1}s^{-1} and $\mu_y^{QFS-BL} = 1927±44$ cm^{2}V^{-1}s^{-1} (Table 1). The THz-CE-OHE data analysis further provided the absolute orientations of the high and low mobility axes for each measurement. A comparison between the orientations of the

---

[1] The use of anisotropic mobility model to fit the data for the ML graphene is done only for consistency and delivers isotropic values within the error bars.

N. Armakavicius, P. Kühne, J. Eriksson et al.

Carbon 172 (2021) 248–259

samples in the AFM and the THz-CE-OHE measurements allowed us to determine the relative orientations of the mobility axes with respect to the surface steps of SiC substrate for the case of QFS-BL EG as exemplified in Fig. 2 (f). The high mobility axes μ_x are determined to be along the surface steps of SiC and the low mobility μ_y axes are perpendicular to the steps, respectively. For the ML EG sample, the angle φ is set according to the orientation determined in the AFM images following the same notations as for QFS-BL EG in the THz-CE-OHE data analysis.

Free charge carrier mobility depends on the effective mass m^* and scattering time τ parameters through the relation $\mu = e\tau/m^*$ (e is the elementary charge). Therefore, anisotropic mobility can be induced by directionally dependent scattering time τ or anisotropic electronic band structure resulting in anisotropic effective mass parameter m^* [53]. The band structure of graphene is well known to have rotational symmetry around the K point and hence the effective mass is isotropic However, anisotropic effective mass in QFS-BL EG may arise from rotational disorder of the two graphene sheets, but this can be ruled out by our micro-LEED investigation indicating no rotational disorder (see Sec. 3.1). In addition, it has been argued that the curvature radius of the graphene sheets over the steps is too high to cause any measurable modification of the band structure [15,22]. Hence, we suggest that the observed mobility anisotropy is caused mainly by directionally dependent carrier scattering time. Any potential contribution from anisotropic effective mass parameter should be negligible and thus, the effective mass parameter was treated as isotropic in our data analysis. We also note that the use of anisotropic effective mass parameter in the model does not improve noticeably the fit to the data compared to the isotropic effective mass model (as reflected by very similar mean square error values for both models). This indicates that no distinguishable anisotropy could be inferred within the experimental uncertainties of the current THz-CE-OHE experiment.

The effective mass parameter for the QFS-BL EG sample determined from THz-CE-OHE data analysis is $0.067(\pm0.002)\ m_0$ and it is in excellent agreement with the effective mass of $0.065\ m_0$ computed from the carrier density using a relation derived from the band curvature in Ref. [54] assuming intermediate energies and band parameters from Ref. [55]. The carrier mobility in the ML EG sample is significantly lower than in the QFS-BL EG and as a consequence the data model analysis is less sensitive to the effective mass parameter. Therefore, in the best-match model for ML EG used to extract the free carrier parameters, shown in Table 1, the effective mass was coupled to the carrier density using the relation reported by Novoselov et al. [52]. In the following subsections, we discuss the potential mechanisms that may cause anisotropic scattering of carriers at the step edges.

3.1. Number of layers and intercalation process

The growth of EG on SiC is enabled by the sublimation of Si at high temperatures with a rate faster than C due to its higher vapor pressure. As the Si atoms leave the surface, the C atoms coalesce and nucleate into graphene layer [56]. However, the sublimation process of Si atoms from the terraces and step edges proceeds with different rates, since the atoms are bonded more weakly in the vicinity of step edges as compared to the terraces. Consequently, Si desorbs from these areas faster and often an extra graphene layer forms at the step edge regions [22]. The larger the step height the larger the number of the C atoms, and thus the higher the probability to form an extra layer. In addition, for the QFS-BL EG case, differences in graphene thickness can also result from inhomogeneous hydrogen intercalation process, since it transforms carbon rich buffer layer into additional graphene layer.
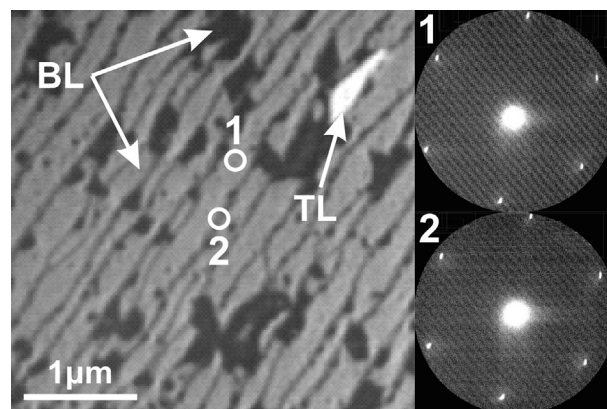

Fig. 3. Representative LEEM and micro-LEED images of QFS-BL EG. Light and dark grey regions[2] (indicated with arrows) correspond to BL, while bright region corresponds to a TL graphene inclusion. Insets 1 and 2 on the right side depict micro-LEED patterns obtained from the terrace (1) and the step edge (2) regions, respectively. Before the measurements sample was annealed at 500 °C for 1 h in ultra-high vacuum.
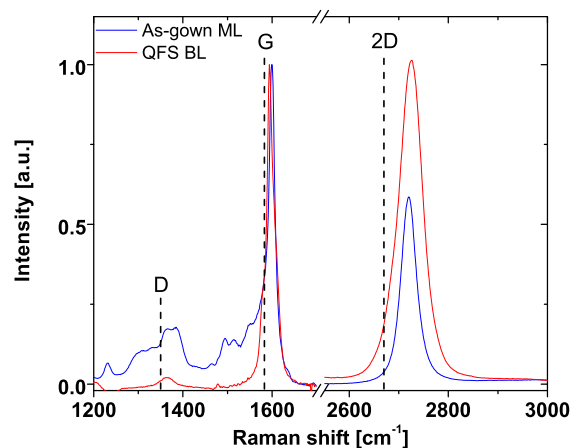

Fig. 4. Averaged Raman scattering spectra for ML [blue] and QFS-BL [red] EG. The spectra are normalized to the respective G-band peaks. The positions of the D, G and 2D-bands of free-standing graphene are indicated by vertical dashed lines. (A colour version of this figure can be viewed online.)

In general, the step edge and the presence of an extra graphene layer represent two different causes of carrier scattering. However, in reality, their effect is often intertwined and hard to disentangle. For all our three sets of samples the step height is typically below 1.5 nm. Reflectivity mapping and LEEM confirmed a homogeneous coverage of SiC with single layer graphene for the ML EG, and BL graphene for the QFS-BL EG samples, respectively (Fig. 1 and Suppl. Inf. Fig. S3). Representative thickness maps obtained from the respective reflectivity maps are presented for the ML and QFS-BL EG samples in Fig. 1 (a) and (b), respectively. Although isolated patches of BL and TL graphene occur in the ML and QFS-BL samples, respectively, the uniformity in graphene coverage for the two samples is 99%. The 1% inhomogeneity in layer thickness cannot account for the observed anisotropy in free hole mobility parameters $\frac{\mu_x}{\mu_y} = 1.25$ of the QFS-BL EG sample. Note that similar 1% inhomogeneity in number of layers is observed for the ML EG sample (Fig. 1 (a)) but no detectable anisotropy in the mobility parameter can be resolved within the experimental error bars (Table 1). Furthermore, in a QFS-BL sample from a different set with layer homogeneity of 92%, a very similar anisotropy in free hole mobility
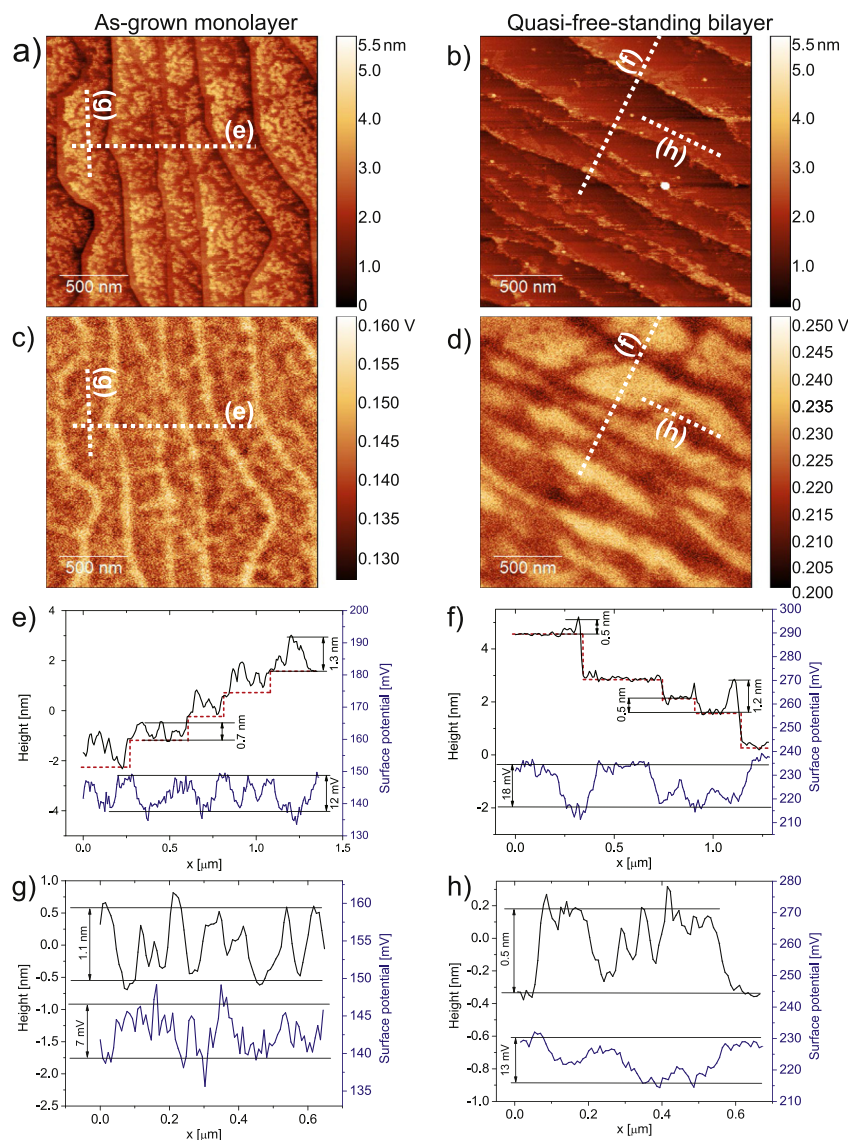
Fig. 5. Representative SKPM images: topography (a) and (b), and surface potential (c) and (d) maps of ML EG (a) and (c), and QFS-BL EG (b) and (d). White dashed lines indicate the height and surface potential profiles taken at the identical positions from the corresponding maps: (g) and (h) at the terraces, and (e) and (f) regions crossing several steps and terraces. The topography profiles are indicated as black solid lines, while the surface potential profiles are indicated as blue solid lines. For height profiles, a terrace flattening procedure was applied. (A colour version of this figure can be viewed online.)

parameters $\frac{\mu_x}{\mu_y} = 1.23$, as for the sample with 99% layer homogeneity, is determined.

In order to further evaluate the uniformity of the intercalation process, we probed different terrace and step edge regions in the QFS-BL EG sample by micro-LEED. Representative LEEM image and micro-LEED diffraction patterns are shown in Fig. 3. The LEEM confirmed that the sample contains BL graphene (grey and dark grey regions[2]) with occasional small TL inclusions (bright white patches). There is no indication of different number of graphene layers at the terraces and step edges. The micro-LEED from the terrace and step edge (regions 1 and 2 in Fig. 3) show identical diffraction patterns with sixfold symmetry typical for EG without a buffer layer below. Moreover, the single sixfold diffraction pattern for BL graphene occurs only when there is no rotational disorder

between the graphene layers in the stack. Thus, a uniform hydrogen intercalation process at the step edges and terraces is realized, resulting in ordered layers of the QFS-BL graphene.

3.2. Defects

To get further insight into defect distribution of the ML and QFS-BL EG samples, we have performed μ−RSI. The Raman spectra normalized to the G-peak and averaged over the measured 5 × 5 μm and 7 × 7 μm μ-RSI maps for ML and QFS-BL EG, respectively, are shown in Fig. 4. The spot size of the probing laser beam is ∼400 nm and thus averaged information over the terrace and step regions is obtained. Nonetheless, important parameters of graphene crystallite size and defects can be deduced by analyzing the D-band at around 1340−1375 cm^{-1}[57−59]. We note that the D-bands of our ML and QFS-BL EG are very weak indicating a high crystalline quality of both EG samples. Raman maps of the 2D-band FWHM and the G peak position indicate highly uniform QFS-BL EG

---

[2] The dark grey color could be associated with physisorbed adsorbates, likely carbon-containing gases, on the BL regions (see Suppl. Inf.).

with respect to doping and strain (Suppl. Inf. Fig. S5). It is worth mentioning that very similar results are obtained for all sample sets. Using the ratio between integrated intensities of the D-band $I(D)$ and G-band $I(G)$ [57], we have estimated an in-plane crystallite size of 430 nm for the QFS-BL EG, which is significantly larger than the average spacing between steps of 340 nm as obtained from the AFM analysis. These results indicate that defects cannot be the main source of the observed anisotropy of free hole mobility parameters for QFS-BL EG. This finding is also in agreement with previous results, showing that EG at the step edges is pristine [26]. For the ML EG, estimation of the crystallites size was not possible since the D-band overlaps with the bands at 1200−1550 cm^{-1} associated with the buffer layer (Fig. 4). Nevertheless, the weak contribution of D-band indicates that defect density is similar to QFS-BL EG sample.

3.3. Interaction with the substrate and ambient

Another potential reason for anisotropic free charge carrier scattering is different interaction between EG and SiC substrate at the terrace and step edge regions. It has been argued that at the step edge the spacing between graphene and the substrate is increased as compared to the respective spacing at the terrace [27]. It was suggested that this leads to almost full depletion of free electrons in the graphene over the step edges and is responsible for the experimentally observed increase in resistance over the step edge [27]. Such a strong variation of doping within the terrace and step edge regions should be manifested in the surface potential maps of ML EG but has not been reported so far. This is mostly due to the fact that there is often a second layer on the step edge, which makes it difficult to discern the effect of the step edge alone. Most often the graphene over the step edge has higher n-type doping (not lower as expected in the above scenario) and the observed difference of surface potential is attributed entirely to the presence of the extra layer [60]. There is only one report showing anisotropic resistance of TL-free QFS-BL EG [30], but no information whether the resistance anisotropy is induced by anisotropic carrier mobility or substrate induced doping variation.

Fig. 5 shows representative SKPM images of the topography (a,b), and the surface potential (c,d) for the ML (a,c) and QFS-BL (b,d) EG samples, respectively. The surface potential and height profiles across the step edges (e,f) and along (g,h) the terrace are also shown in Fig. 5 for both samples. By comparing surface topography and potential maps one can see a clear correlation between the stepped surface morphology and the surface potential variation. This correlation is also manifested in the cross section profiles depicted in Fig. 5 (e), (f) for ML and QFS-BL EG samples, respectively. For the ML EG sample a brighter contrast, i.e. higher surface potential, can be clearly associated with the step edges while the terrace regions show darker contrast, i.e., lower surface potential (Fig. 5 (c)). In contrast, the QFS-BL EG shows the opposite behavior - the surface potential at the step edges is lower (dark contrast) compared to the terrace regions (bright contrast) (Fig. 5 (d)). The average change in surface potential between the step edge and terrace regions is 12 mV and 18 mV for the ML and QFS BL EG, respectively [Fig. 5 (e,f)].

If one assumes that the work-function of the tip is unchanged during the measurement, then the observed variation of the surface potential can be associated with the variation of the graphene work-function. Hence, a higher surface potential can be associated with a lower work-function of the graphene sample [Fig. 5 (c) and (d)]. The work function of a material can be changed by either i) doping through withdrawing (donating) electrons, which lowers (raises) the Fermi level or ii) by the presence of strong dipoles at the surface, e.g., adsorbed species such as water vapor by changing the electron affinity of the material [61]. Considering the first scenario

i) and taking into account that both ML and QFS-BL EG are p-type doped, a lower work-function indicates a lower doping of graphene. Hence, a lower free hole concentration in graphene at the step edges in comparison to the terrace regions of ML EG can be deduced. Vice versa, a higher free hole concentration of QFS-BL EG at the step edges in comparison to the terrace regions may be implied. As mentioned earlier in both ML and QFS-BL EG, environmental doping is the cause for the observed p-type conductivity and thus the scenario with the adsorbed species ii) may also play a role. Indeed, the topography images [Fig. 5 (a) and (b)] reveal the presence of small bright features concentrated at the terrace regions for ML EG and along the step edges for QFS-BL EG, correlating with the dark contrast in the respective surface potential maps [Fig. 5 (c) and (d)]. Since the SKPM measurements were performed at ambient conditions, it is plausible to suggest that the bright features in the topography images are likely to be water vapor adsorbed at the surface. This is further supported by ambient SKPM experiments, in which EG samples, freshly annealed at 500°C in ultra high vacuum conditions, are monitored over time (Suppl. Inf. Fig. S4). Although the graphene surface adsorbs water instantly, tracing the topography and surface potential in clean areas of the sample shows that as the clean surface is gradually covered with the topography features, the bright surface potential contrast disappears (Suppl. Inf. Fig. S4). Our suggestion of adsorbed water causing the bright features in the topography images in Fig. 5 (a) and (b) is also consistent with a much more hydrophilic ML graphene as compared to multilayer graphene [34,62,63]. Hence, we observe here the higher surface coverage with water vapor for our ML than for the QFS-BL EG.

We compared the profile lines of the surface potential maps crossing several terraces containing water film and step edges [Fig. 5 (e), (f)] and profile lines taken at the terraces containing the water film but not crossing any step edges [Fig. 5 (g), (h)]. The terraces contain a water film with varying thickness from 0.5 nm to 1.1 nm for both EG systems. Surface potential variations at the corresponding cross sectional regions of terraces are 7 mV and 13 mV for ML and QFS-BL EG samples, respectively. The observed variation of the surface potential profiles on terraces tend to be lower than variations of profiles taken from step edge and terrace regions (Fig. 5 (e), (f), 12 mV and 18 mV for ML and QFS-BL EG, respectively). This suggests that some variation of the surface potential of 5 mV, associated with step-edge-induced doping, could be present. Assuming that this variation in the surface potential is solely caused by the changes in the graphene work function due to different doping, the variation of p-type doping for QFS-BL EG of 2.8×10^{11} cm^{-2} can be calculated using the relation reported in Ref. [61].

Interestingly, interaction with the substrate is expected to lead to an opposite trend in doping compared to the observed variations in the SKPM in Fig. 5 (c), (d). That is, at the step edges of ML EG, where depletion of free electrons occurs [27], a higher p-type doping may be expected after graphene is being exposed to air, because there are less donor states to be compensated by the ambient acceptor doping. In contrast to this, a lower p-type doping of graphene at the step edges is deduced (bright contrast, i.e., lower work function of graphene, see Fig. 5 (c)). For QFS-BL EG, the p-type doping due to ambient is further enhanced by the substrate spontaneous polarization induced doping. Since the step edges correspond to semi-polar lattice planes $(11\bar{2}n)$ with reduced spontaneous polarization as compared with terraces which have (0001) orientation, a lower p-type doping may be expected for QFS-BL EG on the step edges. Again, our SKPM results show the opposite behavior - a higher p-type doping in graphene is inferred (dark contrast i.e. higher work function of graphene, see Fig. 5 (d)).

Therefore, it is less likely that doping caused by substrate interaction is the main reason for the observed variation of the surface potential. Based on our results, it is plausible to suggest that adsorbed water, which aggregates predominantly at the terrace regions for ML EG and along the step edges for QFS-BL EG is mainly responsible for the observed surface potential differences *via* forming dipoles at the surface and possibly *via* contributing to small extra doping of graphene. However, additional factors such as different surface termination or different stacking-order-induced doping at the step edge and the terrace can contribute to the observed doping variations and need to be further investigated [64].

It has been shown that adsorption of water on graphene can provide scattering centers diminishing the free charge carrier mobility [62]. Therefore, enhanced adsorption of water at the step edges could be the reason for the observed anisotropy of the free hole mobility parameters in QFS-BL EG.[3] In order to evaluate whether this is the case, we have carried out *in-situ* THz-CE-OHE measurements of freshly annealed and clean QFS-BL EG sample. For this purpose, we employed a gas flow cell with controlled inert gases and ambient humidity conditions, which allowed to measure changes of the free charge carrier concentration and mobility parameters [35]. The QFS-BL EG sample was annealed in ultra-high vacuum and then placed in the *in-situ* gas cell for the THz-CE-OHE measurements. Before the measurement, the sample was kept in dry nitrogen environment, which did not show any significant effect on free charge carrier properties. Then the *in-situ* gas cell environment was switched to air with relative humidity of ~80%. The observed changes in free charge carrier properties during the exposure in time window of 260 min are shown in Fig. 6. A p-type doping was detected for the QFS-BL EG sample with free hole sheet density increasing from 6×10^{12} cm^{-2} to 1.2×10^{13} cm^{-2}, which is consistent with previously reported p-type doping caused by ambient gas and water vapor [35]. This change is accompanied by a decrease of free hole mobility parameters along μ_x^{QFS-BL} and across μ_y^{QFS-BL} the steps by roughly 20%. This is in agreement with previous results for QFS-ML EG employing electrical Hall measurements [62]. Most notably, the mobility anisotropy does not vanish or diminish for the freshly annealed QFS-BL EG, as it could be expected if environmental doping causes the anisotropic scattering. On the contrary, the difference between the two in-plane mobility parameters of the freshly annealed sample is even higher compared to the respective values at the end of our *in-situ* experiment (Fig. 6, see also Sec. 3.4. for further discussion). This result indicates that carrier scattering due to adsorbed water vapor, while responsible for the decrease in mobility, cannot be the cause for the observed anisotropy of the free hole mobility parameters of QFS-BL EG.

3.4. Mean free path and intrinsic mobility anisotropy

The measured carrier mobility parameters can be expressed in terms of surface averaged scattering times, where the scattering time along the steps accounts for all intrinsic scattering mechanisms, such as scattering induced by longitudinal acoustic phonons, remote interface phonons, impurities and defects. The scattering time across the steps has an additional term related to the step edges. Assuming Matthessian's rule, the measured mobilities can be written as

$$\mu_x = \frac{e}{m^*}\tau_x;$$
$$\mu_y = \frac{e}{m^*}\tau_y = \frac{e}{m^*}\left(\tau_x^{-1} + \tau_s^{-1}\right)^{-1} \tag{1}$$

e and m^* are unit charge and effective mass parameters, respectively; τ_x is an intrinsic scattering time along the steps and τ_s is a scattering time for the step edges induces scattering. The directional anisotropy of carrier mobility can be expressed as a ratio between the mobility parameters along and across the steps:

$$\frac{\mu_x}{\mu_y} = \left(1 + \frac{\tau_x}{\tau_s}\right) \tag{2}$$

When the scattering associated with the step edges has negligible contribution, τ_s is very long, resulting in a ratio μ_x/μ_y approaching unity and free charge carrier transport is isotropic. The scattering time associated with the step edges, τ_s, can be considered to be a function of the intrinsic scattering time, τ_x, and the average spacing between the steps, w [$\tau_s = f(\tau_x, w)$]. This can be understood by considering the local scattering time in the direction across the step edges. The charge carriers in the middle of the terrace are less affected by the step-edge-induced scattering than the carriers in the vicinity of the step edges. The extent to which the step edge scattering contributes to the total surface averaged scattering time across the steps, τ_y, can be estimated from the ratio l_x/w, where l_x is the intrinsic mean free path ($l_x = v_f\tau_x$, here v_f is a Fermi velocity). When l_x/w is large, the contribution of the step edge scattering is high, and therefore the step edge scattering time, τ_s, becomes short resulting in significant mobility anisotropy ($\mu_x/\mu_y > 1$). The mean-free-path parameters in direction parallel, l_x, and perpendicular, l_y, to the SiC steps calculated from the experimentally determined μ_x, μ_y and N are given in Table 1. In both samples, the average mean free paths are smaller than the average terrace widths, w, determined from AFM analysis to be $w_{ML} = 270$ nm and $w_{QFS-BL} = 340$ nm for the ML and QFS-BLEG, respectively.[4] The ratio l_x/w between the mean free path and the terrace width in QFS-BL EG is about 3 times larger compared to the respective ratio in ML EG [$(l_x/w)^{QFS-BL} \approx 3.1(l_x/w)^{ML}$]. In such case, the contribution of the step edge scattering to the total carrier scattering time in direction across the steps, τ_y, is higher for the QFS-BL EG than for the ML EG ($\tau_s^{QFS-BL} < \tau_s^{ML}$ and $((\mu_x/\mu_y)^{QFS-BL} > (\mu_x/\mu_y)^{ML})$. One can thus hypothesize that the anisotropy of the free hole mobility parameters in QFS-BL EG is manifested as a result of the significantly higher intrinsic mean free paths, l_x (Table 1). The scattering time associated with the steps edge for the QFS-BL EG sample (Table 1), calculated using Equation (1), is $\tau_s = 352$ fs, while the intrinsic scattering time is $\tau_x = 94$ fs. We note that similar results on l_x/w and the respective scattering times were determined for the samples from all sets.

It was previously suggested that dominant scattering mechanisms at room temperature in EG on SiC are the remote interface phonon scattering, as a result of coupling to the polar modes in the substrate, and scattering by impurities [65–67]. Since phonons are thermally generated, the interface phonon scattering is temperature dependent, while the scattering by impurities is considered to be temperature independent [68]. The spacing between graphene

---

[3] In ML EG the step edges are depleted of water (Fig. 5 (a)).

[4] The difference between the terrace widths of the ML and QFS-BLEG samples is not related to hydrogen intercalation. The substrates were cut from different parts of the 4H–SiC 3 inch wafer, and therefore may have a slightly different unintentional off-axis angles resulting in different step spacing.
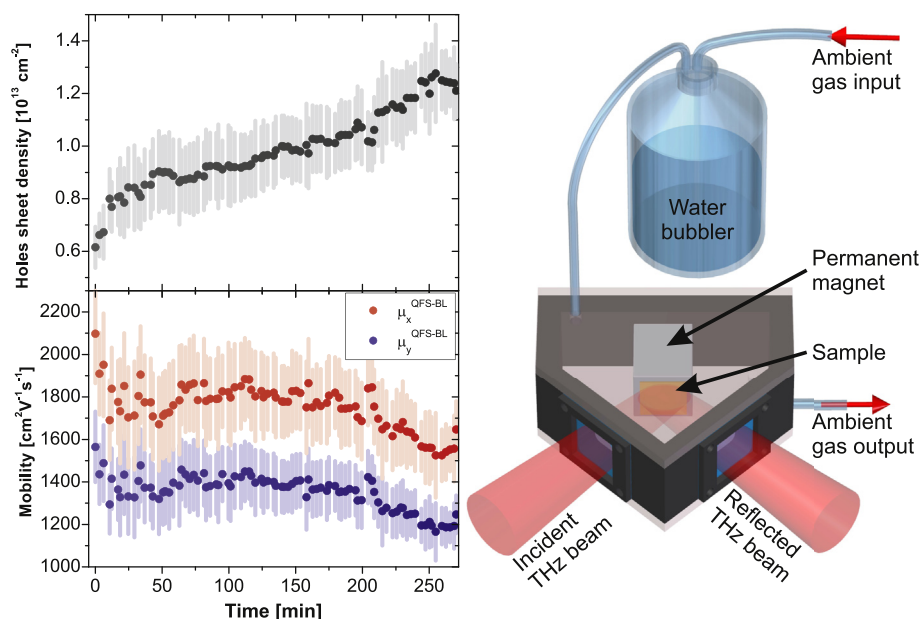
Fig. 6. *In-situ* THz-CE-OHE measurements of the free charge carrier sheet density and mobility parameters along and across the steps in the QFS-BL EG during the exposure to the ambient air and water vapor. Before the measurement, the sample was annealed in ultra-high vacuum and placed in the pure nitrogen environment. (A colour version of this figure can be viewed online.)

and SiC, as well as the surface polarity are different at the terrace and at the step edge regions, which can affect the interface phonon scattering and lead to a variation of the local scattering time. Such a variation will influence the step edge scattering term in the surface averaged scattering time across the steps, τ_y (Eq. (1)), and thus will affect the anisotropy of the measured carrier mobility. On the other hand, at low temperatures interface phonon scattering becomes negligible, thus any variation in local scattering time and the resulting anisotropy, induced by interface phonon scattering, should also become negligible. We thus performed THz-CE-OHE measurements of QFS-BL EG at low temperature of 14 K and room temperature to evaluate the role of interface phonon scattering in the observed free hole anisotropy. The results (Suppl. Inf. Table S1) revealed strong anisotropy of the hole mobility parameter for both temperatures with even higher anisotropy for 14 K as compared to room temperature. These results indicate that phonons do not play a significant role for the observed mobility anisotropy and the scattering is dominated by a temperature independent mechanism(s).

We further note that we observe mobility anisotropy in the freshly annealed QFS-BL EG with a free hole density of 5.92×10^{12} cm^{-2} (Suppl. Inf. Table S1), which is the intrinsic p-type doping induced only by the spontaneous polarization of the substrate [18,49,50]. This result is in agreement with the *in-situ* THz-CE-OHE experiments in Fig. 6 and further confirms that the origin of the observed anisotropy is not related to the ambient doping. Even more, the mobility anisotropy is 60% for intrinsic QFS-BL EG (Suppl. Inf. Table S1) compared to 25% for the case of ambient-doped QFS-BL EG with free hole density of 1.014×10^{13} cm^{-2} (Table 1). Such a variation of the anisotropy magnitude could be explained in view of its dependence on the mean free path (see discussion above). The latter is affected by the values of the free hole density (i.e. also the effective mass) and thus by sample history. We also note that the resistivity anisotropy of TL-free QFS-BL EG of 37%, reported previously [30], lies well within the range of mobility anisotropy we find.

In summary, the step edges introduce inherent scattering (τ_s)

that is not related to additional defects, presence of an extra graphene layer/layers nor variation of ambient doping (see subsections 3.1, 3.2 and 3.3) and it is virtually temperature independent. We suggest that τ_s is related to the temperature independent Coulomb scattering induced by surface charges of the substrate or/and strain in graphene due to bending that causes potential barrier for carrier scattering, as theoretically proposed for ML EG [27]. Additional factors such as different surface termination or different stacking-order-induced doping at the step edge and the terrace [64] can contribute to the observed doping variations and serve as a source of scattering. Such an intrinsic step-induced scattering is expected also in the case of ML EG but remains hidden as a result of the reduced mean free path parameters (Table 1). We also note that as room-temperature mobility parameters of ML EG reported in the literature are typically in the range of 1000–1500 cm^{2}V^{-1}s^{-1}, e.g. Ref. [3,29,30], the intrinsic mobility anisotropy in homogeneous ML EG or QFS ML EG may be difficult to detect in general due to a reduced mean free path with respect to terrace width. This provides potential explanation for the observed differences between nanoscale and macroscopic techniques reporting isotropic mobility parameters in ML EG from electrical Hall bar measurements and the increase in resistance over the step edge *via* local conductance mapping [3,17,25,28]. Based on our results, we suggest that the mean-free path should be taken into account when considering the effect of the step height [27,29,30]. It is important to note that although hydrogen intercalation reduces the interaction with the substrate and increases the free charge carrier mobility parameters in graphene, it does not amend the step-induced scattering. This result implies that potential applications of QFS graphene on SiC may require technological developments ensuring sufficiently large terrace widths and aligning of device structures. In this respect, it is interesting to mention the optimization of growth conditions to suppress step bunching [30] and the possibility to localize step bunching by employing a capping technique [69]. The latter, in particular, allows to pin the steps and ensures aligned step-free regions [69]. On the other hand, the directionally dependent free hole mobility in QFS-BL graphene

also opens opportunities for novel applications such as in-plane anisotropic field effect transistors and neuromorphic devices [70].

4. Conclusions

The THz-CE-OHE is demonstrated to be an excellent tool to determine directional dependent free charge carrier properties in 2D materials with ML and QFS-BL EG as examples. Both, ML and QFS-BL EG are found to exhibit p-type conductivity as a result of an ambient acceptor doping. The free hole density in QFS-BL EG is shown to increase with $\sim 7 \times 10^{12}$ cm^{-2} in comparison with ML EG, which is consistent with enhanced p-type doping induced by the spontaneous polarization of the SiC. The ML EG is found to exhibit isotropic free hole mobility parameters. In contrast, a strong anisotropy of free hole mobility is revealed for both freshly annealed (substrate doped only) and ambient doped QFS-BL EG with higher mobility parameters along the SiC steps and a lower mobility parameters in direction perpendicular to the SiC steps. Despite the increased free charge carrier density in QFS-BL EG, the hole mobility parameters are larger by a factor of two compared to those in ML EG as a result of reduced interaction with the substrate. We have shown that presence of defects and extra layers, interface phonon scattering as well as substrate and ambient induced doping can be ruled out as possible causes for the observed anisotropy of free hole mobility in QFS-BL EG. Instead, we suggest that the step edge introduces intrinsic scattering related to the temperature-independent Coulomb scattering induced by charged impurities or/and strain in graphene due to bending that causes potential barrier for carrier scattering, and the anisotropy of the free charge mobility parameters in QFS-BL EG is manifested as a result of the significantly increased ratio between mean free path and average terrace width parameters. Such an intrinsic step-induced scattering is expected also in the case of ML EG but remains hidden as a result of the typically reported reduced mobility parameters. This scenario provides a potential explanation for the observed differences between nanoscale and macroscopic techniques reporting isotropic mobility parameters in ML EG from electrical Hall bar measurements and the increase in resistance over the step edge *via* local conductance mapping [3,17,25,28]. It is important to note that although hydrogen intercalation reduces the interaction with the substrate and increases the free charge carrier mobility parameters in EG, it does not eliminate the step induced scattering. This result has significant implications for the potential applications of QFS EG in current and future electronic devices.

Declaration of competing interest

The authors declare that they have no known competing financial interests or personal relationships that could have appeared to influence the work reported in this paper.

Acknowledgement

Appendix A. Supplementary data

Supplementary data to this article can be found online at https://doi.org/10.1016/j.carbon.2020.09.035.

References

[1] K.S. Novoselov, A.K. Geim, S.V. Morozov, D. Jiang, Y. Zhang, S.V. Dubonos, I.V. Grigorieva, A.A. Firsov, Electric field effect in atomically thin carbon films, Science 306 (5696) (2004) 666–669, https://doi.org/10.1126/science.1102896.

[2] K.S. Novoselov, V. Fal, L. Colombo, P. Gellert, M. Schwab, K. Kim, et al., A roadmap for graphene, Nature 490 (7419) (2012) 192. https://www.nature.com/articles/nature11458.

[3] T. Yager, A. Lartsev, R. Yakimova, S. Lara-Avila, S. Kubatkin, Wafer-scale homogeneity of transport properties in epitaxial graphene on SiC, Carbon 87 (2015) 409–414, https://doi.org/10.1016/j.carbon.2015.02.058.

[4] C. Dimitrakopoulos, Y.-M. Lin, A. Grill, D.B. Farmer, M. Freitag, Y. Sun, S.-J. Han, Z. Chen, K.A. Jenkins, Y. Zhu, Z. Liu, T.J. McArdle, J.A. Ott, R. Wisnieff, P. Avouris, Wafer-scale epitaxial graphene growth on the si-face of hexagonal SiC (0001) for high frequency transistors, J. Vac. Sci. Technol., B 28 (5) (2010) 985–992, https://doi.org/10.1116/1.3480961.

[5] C. Virojanadara, M. Syväjarvi, R. Yakimova, L.I. Johansson, A.A. Zakharov, T. Balasubramanian, Homogeneous large-area graphene layer growth on $6h$-sic(0001), Phys. Rev. B 78 (2008), https://doi.org/10.1103/PhysRevB.78.245403.

[6] K.V. Emtsev, A. Bostwick, K. Horn, J. Jobst, G.L. Kellogg, L. Ley, J.L. McChesney, T. Ohta, S.A. Reshanov, J. Röhrl, et al., Towards wafer-size graphene layers by atmospheric pressure graphitization of silicon carbide, Nat. Mater. 8 (3) (2009), https://doi.org/10.1038/nmat2382.

[7] P.K. Ang, W. Chen, A.T.S. Wee, K.P. Loh, Solution-gated epitaxial graphene as pH sensor, J. Am. Chem. Soc. 130 (44) (2008) 14392–14393, https://doi.org/10.1021/ja805090z.

[8] Y.-M. Lin, C. Dimitrakopoulos, K.A. Jenkins, D.B. Farmer, H.-Y. Chiu, A. Grill, P. Avouris, 100-Ghz transistors from wafer-scale epitaxial graphene, Science 327 (5966) (2010), https://doi.org/10.1126/science.1184289, 662–662.

[9] Y.-M. Lin, A. Valdes-Garcia, S.-J. Han, D.B. Farmer, I. Meric, Y. Sun, Y. Wu, C. Dimitrakopoulos, A. Grill, P. Avouris, et al., Wafer-Scale Graphene Integrated Circuit, Science 332 (6035) (2011) 1294–1297, https://doi.org/10.1126/science.1204428.

[10] M. Rodner, J. Bahonjic, M. Mathisen, R. Gunnarsson, S. Ekeroth, U. Helmersson, I.G. Ivanov, R. Yakimova, J. Eriksson, Performance tuning of gas sensors based on epitaxial graphene on silicon carbide, Mater. Des. 153 (2018) 153–158, https://doi.org/10.1016/j.matdes.2018.04.087.

[11] N.O. Weiss, H. Zhou, L. Liao, Y. Liu, S. Jiang, Y. Huang, X. Duan, Graphene: an emerging electronic material, Adv. Mater. 24 (43) (2012) 5782–5825, https://doi.org/10.1002/adma.201201482.

[12] T. Ohta, A. Bostwick, T. Seyller, K. Horn, E. Rotenberg, Controlling the electronic structure of bilayer graphene, Science 313 (5789) (2006) 951–954, https://doi.org/10.1126/science.1130681.

[13] C. Riedl, A.A. Zakharov, U. Starke, Precise *in situ* thickness analysis of epitaxial graphene layers on SiC(0001) using low-energy electron diffraction and angle resolved ultraviolet photoelectron spectroscopy, Appl. Phys. Lett. 93 (3) (2008) 033106, https://doi.org/10.1063/1.2960341.

[14] J.L. Tedesco, B.L. VanMil, R.L. Myers-Ward, J.M. McCrate, S.A. Kitt, P.M. Campbell, G.G. Jernigan, J.C. Culbertson, C.R. Eddy, D.K. Gaskill, Hall effect mobility of epitaxial graphene grown on silicon carbide, Appl. Phys. Lett. 95 (12) (2009) 122102, https://doi.org/10.1063/1.3224887.

[15] M.K. Yakes, D. Gunlycke, J.L. Tedesco, P.M. Campbell, R.L. Myers-Ward, C.R. Eddy, D.K. Gaskill, P.E. Sheehan, A.R. Laracuente, Conductance anisotropy in epitaxial graphene sheets generated by substrate interactions, Nano Lett. 10 (5) (2010) 1559–1562, https://doi.org/10.1021/nl9035302.

[16] R. Yakimova, T. Iakimov, G. Yazdi, C. Bouhafs, J. Eriksson, A. Zakharov,

A. Boosalis, M. Schubert, V. Darakchieva, Morphological and electronic properties of epitaxial graphene on SiC, Phys. B Condens. Matter 439 (2014) 54–59, https://doi.org/10.1016/j.physb.2013.12.048.

[17] S.-H. Ji, J. Hannon, R. Tromp, V. Perebeinos, J. Tersoff, F. Ross, Atomic-scale transport in epitaxial graphene, Nat. Mater. 11 (2) (2012) 114–119. https://www.nature.com/articles/nmat3170.

[18] C. Riedl, C. Coletti, T. Iwasaki, A.A. Zakharov, U. Starke, Quasi-Free-Standing Epitaxial Graphene on SiC Obtained by Hydrogen Intercalation, Phys. Rev. Lett 103 (24) (2009) 246804, https://doi.org/10.1103/PhysRevLett.103.246804.

[19] Y. Zhang, T.-T. Tang, C. Girit, Z. Hao, M.C. Martin, A. Zettl, M.F. Crommie, Y.R. Shen, F. Wang, Direct observation of a widely tunable bandgap in bilayer graphene, Nature 459 (7248) (2009) 820–823. https://www.nature.com/articles/nature08105.

[20] B. Jouault, B. Jabakhanji, N. Camara, W. Desrat, A. Tiberj, J.-R. Huntzinger, C. Consejo, A. Caboni, P. Godignon, Y. Kopelevich, J. Camassel, Probing the electrical anisotropy of multilayer graphene on the si face of 6H-SiC, Phys. Rev. B 82 (8) (2010) 085438, https://doi.org/10.1103/PhysRevB.82.085438, 085438.

[21] S. Odaka, H. Miyazaki, S.-L. Li, A. Kanda, K. Morita, S. Tanaka, Y. Miyata, H. Kataura, K. Tsukagoshi, Y. Aoyagi, Anisotropic transport in graphene on SiC substrate with periodic nanofacets, Appl. Phys. Lett 96 (6) (2010) 062111, https://doi.org/10.1063/1.3309701.

[22] T. Ciuk, S. Cakmakyapan, E. Ozbay, P. Caban, K. Grodecki, A. Krajewska, I. Pasternak, J. Szmidt, W. Strupinski, Step-edge-induced resistance anisotropy in quasi-free-standing bilayer chemical vapor deposition graphene on SiC, J. Appl. Phys. 116 (12) (2014) 123708, https://doi.org/10.1063/1.4896581.

[23] M. Kruskopf, K. Pierz, S. Wundrack, R. Stosch, T. Dziomba, C.-C. Kalmbach, A. Müller, J. Baringhaus, C. Tegenkamp, F.J. Ahlers, H.W. Schumacher, Epitaxial graphene on SiC: modification of structural and electron transport properties by substrate pretreatment, J. Phys. Condens. Matter 27 (18) (2015) 185303, https://doi.org/10.1088/0953-8984/27/18/185303.

[24] A. Endo, F. Komori, K. Morita, T. Kajiwara, S. Tanaka, Highly anisotropic parallel conduction in the stepped substrate of epitaxial graphene grown on vicinal sic, J. Low Temp. Phys 179 (3) (2015) 237–250, https://doi.org/10.1007/s10909-015-1277-y.

[25] F. Giannazzo, I. Deretzis, A. La Magna, F. Roccaforte, R. Yakimova, Electronic transport at monolayer-bilayer junctions in epitaxial graphene on SiC, Phys. Rev. B 86 (23) (2012) 235422, https://doi.org/10.1103/PhysRevB.86.235422.

[26] S.-H. Bae, X. Zhou, S. Kim, Y.S. Lee, S.S. Cruz, Y. Kim, J.B. Hannon, Y. Yang, D.K. Sadana, F.M. Ross, H. Park, J. Kim, Unveiling the carrier transport mechanism in epitaxial graphene for forming wafer-scale, single-domain graphene, Proc. Natl. Acad. Sci. U.S.A. 114 (16) (2017) 4082–4086, https://doi.org/10.1073/pnas.1620176114.

[27] T. Low, V. Perebeinos, J. Tersoff, P. Avouris, Deformation and scattering in graphene over substrate steps, Phys. Rev. Lett. 108 (9) (2012) 096601, https://doi.org/10.1103/PhysRevLett.108.096601, 096601.

[28] D. Momeni Pakdehi, J. Aprojanz, A. Sinterhauf, K. Pierz, M. Kruskopf, P. Willke, J. Baringhaus, J. Stöckmann, G. Traeger, F. Hohls, et al., Minimum resistance anisotropy of epitaxial graphene on SiC, ACS Appl. Mater. Interfaces 10 (6) (2018) 6039–6045, https://doi.org/10.1021/acsami.7b18641.

[29] A. Sinterhauf, G.A. Traeger, D.M. Pakdehi, P. Schädlich, P. Willke, F. Speck, T. Seyller, C. Tegenkamp, K. Pierz, H.W. Schumacher, et al., Substrate induced nanoscale resistance variation in epitaxial graphene, Nat. Commun. 11 (2020), https://doi.org/10.1038/s41467-019-14192-0.

[30] D. Momeni Pakdehi, K. Pierz, S. Wundrack, J. Aprojanz, T.T.N. Nguyen, T. Dziomba, F. Hohls, A. Bakin, R. Stosch, C. Tegenkamp, et al., Homogeneous large-area quasi-free-standing monolayer and bilayer graphene on SiC, ACS Applied Nano Materials 2 (2) (2019) 844–852, https://doi.org/10.1021/acsanm.8b02093.

[31] T. Hofmann, A. Boosalis, P. Kühne, C.M. Herzinger, J.A. Woollam, D.K. Gaskill, J.L. Tedesco, M. Schubert, Hole-channel conductivity in epitaxial graphene determined by terahertz optical-hall effect and midinfrared ellipsometry, Appl. Phys. Lett. 98 (4) (2011) 041906, https://doi.org/10.1063/1.3548543.

[32] P. Kühne, V. Darakchieva, R. Yakimova, J.D. Tedesco, R.L. Myers-Ward, C.R. Eddy, D.K. Gaskill, C.M. Herzinger, J.A. Woollam, M. Schubert, T. Hofmann, Polarization selection rules for inter-landau-level transitions in epitaxial graphene revealed by the infrared optical hall effect, Phys. Rev. Lett. 111 (7) (2013) 077402, https://doi.org/10.1103/PhysRevLett.111.077402, 077402.

[33] C. Bouhafs, V. Stanishev, A.A. Zakharov, T. Hofmann, P. Kühne, T. Iakimov, R. Yakimova, M. Schubert, V. Darakchieva, Decoupling and ordering of multilayer graphene on c-face 3C-SiC(111), Appl. Phys. Lett. 109 (20) (2016) 203102, https://doi.org/10.1063/1.4967525.

[34] N. Armakavicius, C. Bouhafs, V. Stanishev, P. Kühne, R. Yakimova, S. Knight, T. Hofmann, M. Schubert, V. Darakchieva, Cavity-enhanced optical Hall effect in epitaxial graphene detected at terahertz frequencies, Appl. Surf. Sci. 421 (2017) 357–360, https://doi.org/10.1016/j.apsusc.2016.10.023.

[35] S. Knight, T. Hofmann, C. Bouhafs, N. Armakavicius, P. Kühne, V. Stanishev, I.G. Ivanov, R. Yakimova, S. Wimer, M. Schubert, et al., In-situ terahertz optical hall effect measurements of ambient effects on free charge carrier properties of epitaxial graphene, Sci. Rep. 7 (1) (2017) 1–8, https://doi.org/10.1038/s41598-017-05333-w.

[36] C. Bouhafs, A. Zakharov, I. Ivanov, F. Giannazzo, J. Eriksson, V. Stanishev, P. Kühne, T. Iakimov, T. Hofmann, M. Schubert, F. Roccaforte, R. Yakimova, V. Darakchieva, Multi-scale investigation of interface properties, stacking order and decoupling of few layer graphene on C-face 4H-SiC, Carbon 116

(2017) 722–732, https://doi.org/10.1016/j.carbon.2017.02.026. http://www.sciencedirect.com/science/article/pii/S0008622317301549.

[37] P. Kühne, N. Armakavicius, V. Stanishev, C.M. Herzinger, M. Schubert, V. Darakchieva, Advanced terahertz frequency-domain ellipsometry instrumentation for in situ and ex situ applications, IEEE Transactions on Terahertz Science and Technology 8 (3) (2018) 257–270, https://doi.org/10.1109/TTHZ.2018.2814347. https://ieeexplore.ieee.org/document/8331870.

[38] I. Persson, N. Armakavicius, C. Bouhafs, V. Stanishev, P. Kühne, T. Hofmann, M. Schubert, J. Rosen, R. Yakimova, P.O.A. Persson, V. Darakchieva, Origin of layer decoupling in ordered multilayer graphene grown by high-temperature sublimation on C-face 4H-SiC, APL Mater. 8 (1) (2020) 011104, https://doi.org/10.1063/1.5134862.

[39] S. Knight, S. Schöche, P. Kühne, T. Hofmann, V. Darakchieva, M. Schubert, Tunable cavity-enhanced terahertz frequency-domain optical Hall effect, Rev. Sci. Instrum. 91 (8) (2020) 083903, https://doi.org/10.1063/5.0010267.

[40] T. Hofmann, P. Kühne, S. Schöche, J.-T. Chen, U. Forsberg, E. Janzén, N. Ben Sedrine, C.M. Herzinger, J.A. Woollam, M. Schubert, V. Darakchieva, Temperature dependent effective mass in algan/gan high electron mobility transistor structures, Appl. Phys. Lett. 101 (19) (2012) 192102, https://doi.org/10.1063/1.4765351.

[41] N. Armakavicius, J.-T. Chen, T. Hofmann, S. Knight, P. Kühne, D. Nilsson, U. Forsberg, E. Janzén, V. Darakchieva, Properties of two-dimensional electron gas in AlGaN/GaN HEMT structures determined by cavity-enhanced thz optical Hall effect, Phys. Status Solidi C 13 (5–6) (2016) 369–373, https://doi.org/10.1002/pssc.201510214.

[42] S. Knight, S. Schöche, V. Darakchieva, P. Kühne, J.-F. Carlin, N. Grandjean, C.M. Herzinger, M. Schubert, T. Hofmann, Cavity-enhanced optical hall effect in two-dimensional free charge carrier gases detected at terahertz frequencies, Opt. Lett. 40 (12) (2015) 2688–2691, https://doi.org/10.1364/OL.40.002688.

[43] M. Schubert, P. Kühne, V. Darakchieva, T. Hofmann, Optical Hall effect-model description: tutorial, Journal of the Optical Society of America A 33 (8) (2016) 1553–1568, https://doi.org/10.1364/JOSAA.33.001553. http://josaa.osa.org/abstract.cfm?URI=josaa-33-8-1553.

[44] C. Bouhafs, Structural and Electronic Properties of Graphene on 4H-and 3C-SiC, Linköping University Electronic Press, 2016. Linköping Studies in Science and Technology, Dissertations, ISSN 0345-7524, https://doi.org/10.3384/diss.diva-132408.

[45] H. Kageshima, H. Hibino, H. Yamaguchi, M. Nagase, Stability and reactivity of steps in the initial stage of graphene growth on the SiC(0001) surface, Phys. Rev. B 88 (23) (2013) 235405, https://doi.org/10.1103/PhysRevB.88.235405.

[46] I.G. Ivanov, J.U. Hassan, T. Iakimov, A.A. Zakharov, R. Yakimova, E. Janzén, Layer-number determination in graphene on SiC by reflectance mapping, Carbon 77 (2014) 492–500, https://doi.org/10.1016/j.carbon.2014.05.054.

[47] M. Schubert, T. Hofmann, C.M. Herzinger, Generalized far-infrared magneto-optic ellipsometry for semiconductor layer structures: determination of free-carrier effective-mass, mobility, and concentration parameters in n-type GaAs, J. Opt. Soc. Am. A 20 (2) (2003) 347–356, https://doi.org/10.1364/JOSAA.20.000347.

[48] A.N. Sidorov, K. Gaskill, M. Buongiorno Nardelli, J.L. Tedesco, R.L. Myers-Ward, C.R. Eddy, T. Jayasekera, K.W. Kim, R. Jayasingha, A. Sherehiy, R. Stallard, G.U. Sumanasekera, Charge transfer equilibria in ambient-exposed epitaxial graphene on (000-1) 6H-SiC, J. Appl. Phys. 111 (11) (2012) 113706, https://doi.org/10.1063/1.4725413.

[49] J. Ristein, S. Mammadov, T. Seyller, Origin of doping in quasi-free-standing graphene on silicon carbide, Phys. Rev. Lett. 108 (24) (2012) 246104, https://doi.org/10.1103/PhysRevLett.108.246104.

[50] S. Mammadov, J. Ristein, R.J. Koch, M. Ostler, C. Raidel, M. Wanke, R. Vasiliauskas, R. Yakimova, T. Seyller, Polarization doping of graphene on silicon carbide, 2D Mater. 1 (3) (2014) 035003, https://doi.org/10.1088/2053-1583/1/3/035003.

[51] C. Riedl, C. Coletti, U. Starke, Structural and electronic properties of epitaxial graphene on SiC(0001): a review of growth, characterization, transfer doping and hydrogen intercalation, J. Phys. Appl. Phys 43 (37) (2010) 374009, https://doi.org/10.1088/0022-3727/43/37/374009.

[52] K.S. Novoselov, A.K. Geim, S.V. Morozov, D. Jiang, M.I. Katsnelson, I.V. Grigorieva, S.V. Dubonos, A.A. Firsov, Two-dimensional gas of massless Dirac fermions in graphene, Nature 438 (7065) (2005) 197–200, https://doi.org/10.1038/nature04233.

[53] V. Ariel, A. Natan, Electron effective mass in graphene, in: 2013 International Conference on Electromagnetics in Advanced Applications (ICEAA), IEEE, 2013, pp. 696–698, https://doi.org/10.1109/ICEAA.2013.6632334.

[54] E. McCann, M. Koshino, The electronic properties of bilayer graphene, Rep. Prog. Phys. 76 (5) (2013) 056503, https://doi.org/10.1088/0034-4885/76/5/056503.

[55] K. Zou, X. Hong, J. Zhu, Effective mass of electrons and holes in bilayer graphene: electron-hole asymmetry and electron-electron interaction, Phys. Rev. B 84 (8) (2011) 085408, https://doi.org/10.1103/PhysRevB.84.085408, 085408.

[56] G.R. Yazdi, R. Vasiliauskas, T. Iakimov, A. Zakharov, M. Syväjärvi, R. Yakimova, Growth of large area monolayer graphene on 3C-SiC and a comparison with other SiC polytypes, Carbon 57 (2013) 477–484, https://doi.org/10.1016/j.carbon.2013.02.022. http://www.sciencedirect.com/science/article/pii/S0008622313001528.

[57] M.A. Pimenta, G. Dresselhaus, M.S. Dresselhaus, L.G. Cançado, A. Jorio, R. Saito, Studying disorder in graphite-based systems by Raman spectroscopy, Phys.

Chem. Chem. Phys. 9 (2007) 1276—1290, https://doi.org/10.1039/B613962K.

[58] L.G. Cançado, A. Jorio, E.H.M. Ferreira, F. Stavale, C.A. Achete, R.B. Capaz, M.V.O. Moutinho, A. Lombardo, T.S. Kulmala, A.C. Ferrari, Quantifying defects in graphene via Raman spectroscopy at different excitation energies, Nano Lett. 11 (8) (2011) 3190—3196, https://doi.org/10.1021/nl201432g.

[59] A. Tiberj, J.-R. Huntzinger, J. Camassel, F. Hiebel, A. Mahmood, P. Mallet, C. Naud, J.-Y. Veuillen, Multiscale investigation of graphene layers on 6H-SiC(000-1), Nanoscale Res. Lett. 6 (1) (2011) 171, https://doi.org/10.1186/1556-276X-6-171.

[60] C. Melios, V. Panchal, C.E. Giusca, W. Strupiński, S.R.P. Silva, O. Kazakova, Carrier type inversion in quasi-free standing graphene: studies of local electronic and structural properties, Sci. Rep. 5 (2015) 10505, https://doi.org/10.1038/srep10505.

[61] R. Pearce, J. Eriksson, T. Iakimov, L. Hultman, A. Lloyd Spetz, R. Yakimova, On the differing sensitivity to chemical gating of single and double layer epitaxial graphene explored using scanning kelvin probe microscopy, ACS Nano 7 (5) (2013) 4647—4656, https://doi.org/10.1021/nn3052633.

[62] C. Melios, C.E. Giusca, V. Panchal, O. Kazakova, Water on graphene: review of recent progress, 2D Mater. 5 (2) (2018) 022001, https://doi.org/10.1088/2053-1583/aa9ea9.

[63] C. Melios, M. Winters, W. Strupiński, V. Panchal, C.E. Giusca, K.D.G. Imalka Jayawardena, N. Rorsman, S.R.P. Silva, O. Kazakova, Tuning epitaxial graphene sensitivity to water by hydrogen intercalation, Nanoscale 9 (2017) 3440—3448, https://doi.org/10.1039/C6NR09465A.

[64] D.M. Pakdehi, P. Schädlich, T.T.N. Nguyen, A.A. Zakharov, S. Wundrack, F. Speck, K. Pierz, T. Seyller, C. Tegenkamp, H.W. Schumacher, Silicon carbide stacking-order-induced doping variation in epitaxial graphene, Adv. Funct. Mater. (2020) 2004695, https://doi.org/10.1002/adfm.202004695.

[65] S. Fratini, F. Guinea, Substrate-limited electron dynamics in graphene, Phys. Rev. B 77 (19) (2008) 195415, https://doi.org/10.1103/PhysRevB.77.195415.

[66] S. Tanabe, Y. Sekine, H. Kageshima, M. Nagase, H. Hibino, Carrier transport mechanism in graphene on SiC(0001), Phys. Rev. B 84 (11) (2011) 115458, https://doi.org/10.1103/PhysRevB.84.115458.

[67] S. Lisesivdin, G. Atmaca, E. Arslan, S. Çakmakyapan, Ö. Kazar, S. Bütün, J. Ul-Hassan, E. Janzén, E. Özbay, Extraction and scattering analyses of 2D and bulk carriers in epitaxial graphene-on-SiC structure, Phys. E Low-dimens. Syst. Nanostruct. 63 (2014) 87—92, https://doi.org/10.1016/j.physe.2014.05.016.

[68] M. Winters, J. Hassan, H. Zirath, E. Janzén, N. Rorsman, A temperature dependent measurement of the carrier velocity vs. electric field characteristic for as-grown and h-intercalated epitaxial graphene on SiC, J. Appl. Phys. 113 (19) (2013) 193708, https://doi.org/10.1063/1.4807162.

[69] J. Palmer, J. Kunc, Y. Hu, J. Hankinson, Z. Guo, C. Berger, W.A. de Heer, Controlled epitaxial graphene growth within removable amorphous carbon corrals, Appl. Phys. Lett. 105 (2) (2014) 023106, https://doi.org/10.1063/1.4890499.

[70] L. Liang, W. Han, P. Lejing, N. Ping, H. Junbo, W. Chengliang, S. Bin, L. Huiqiao, X. Jie, B. Yoshio, Z. Tianyou, Emerging in-plane anisotropic two-dimensional materials, InfoMat 1 (1) (2019) 54—73, https://doi.org/10.1002/inf2.12005.